

Invited Research Article

Coexisting Strombolian and Hawaiian activity during the 2018 fissure eruption of Kīlauea – Implications for processes of weak explosions[☆]



Brett Halsey Walker^{a,*}, Bruce F. Houghton^a, Edward W. Llewellyn^b

^a Department of Earth Sciences, University of Hawai'i, Honolulu, Hawai'i 96822, USA

^b Department of Earth Sciences, Science Labs, Durham University, Durham DH1 3LE, UK

ARTICLE INFO

Keywords:

Eruption style
Explosive volcanism
Fissure
Fountain
Kīlauea
Strombolian

ABSTRACT

Mildly explosive eruptions—the most frequent manifestations of subaerial explosive volcanism on Earth—broadly group into two styles: Strombolian and Hawaiian. The former is characterized by sequences of intermittent discrete explosions, and the latter by sustained pyroclastic fountaining. Explosive activity during the 2018 fissure eruption of Kīlauea volcano (Hawai'i) provided an exceptional opportunity to record a wide range of Strombolian and Hawaiian behavior. We used high-resolution videography and image processing to quantify the frequency, duration, and steadiness (as seen by fluctuation in maximum clast height) of Hawaiian fountains and Strombolian jets. Combining these data with the currently published understanding of two-phase flow (melt + bubbles), we propose that the diversity in eruptive styles is related to melt viscosity, changing mass flux, and the extent of mechanical coupling versus decoupling of the exsolving volatile phases from the host magma. In particular, we single out the effects of the contrasts in abundance of a sub-population of the largest (meter-scale) bubbles that emerge intermittently and independently through the magma in the vent. The coexistence of these styles—at vents often only meters apart—is a clear indication that the diversity in eruptive behavior is modulated at depths of probably no more than 100 m and perhaps as shallow as tens of meters.

1. Introduction

1.1. Weak explosive eruptions

Weak explosive eruptions have mass discharge rates that are generally $<10^5 \text{ kg s}^{-1}$ (Taddeucci et al., 2015; Houghton et al., 2016) and typically form locally dispersed scoria cones and ramparts. Despite their relatively low explosivity, they nonetheless pose a substantial hazard to people and infrastructure because they are the most common form of subaerial eruptions (Taddeucci et al., 2015), they may occur in close proximity to human populations (Neal et al., 2018), and they are highly dynamic, showing rapid shifts in style and intensity (e.g., Gurioli et al., 2008; Ripepe et al., 2008; Gaudin et al., 2017; Houghton et al., 2020). There are two archetypal styles of weak explosive activity: Strombolian (Mercalli, 1881), and Hawaiian (Macdonald, 1972). Strombolian activity is normally characterized by brief, impulsive explosive events (lasting up to tens of seconds) that eject pulses of incandescent pyroclastic material and volcanic gases; Hawaiian activity is characterized by much longer episodes (often hours-days) of sustained pyroclastic

fountaining (e.g., Houghton and Gonnermann, 2008; Taddeucci et al., 2015; Houghton et al., 2016). Studies involving analog laboratory experiments and/or numerical conduit models explain the difference between these two styles in terms of contrasting regimes of two-phase flow in volcanic conduits (Fig. 1; James et al., 2013; Jaupart and Vergniolle, 1988; Parfitt, 2004). In these models, Strombolian activity is thought to be driven by ascent and bursting of large bubble slugs or clusters that are decoupled from the melt, whereas Hawaiian activity is driven by the buoyancy provided by smaller bubbles that are coupled to the melt (see references above and Taddeucci et al., 2015).

Descriptions and interpretations of behaviors that fall between Hawaiian and Strombolian are rare, partly because eruptions from point-source vents are usually dominated by one major eruptive style (e.g., Hawaiian fountaining at Pu'u 'O'o (Hawaii, USA) from 1983 to 1986, and Strombolian explosions at Erebus (Antarctica) and Stromboli (Italy)). Exceptions have been recorded at Etna (e.g., Calvari et al., 2011, 2018; Andronico et al., 2021) and during the 2018 LERZ eruption at Kīlauea (Houghton et al., 2020).

There are, as yet, insufficient systematic quantitative observations of

[☆] Article invited 19 Sep 2019.

* Corresponding author.

E-mail address: junobhw@gmail.com (B.H. Walker).

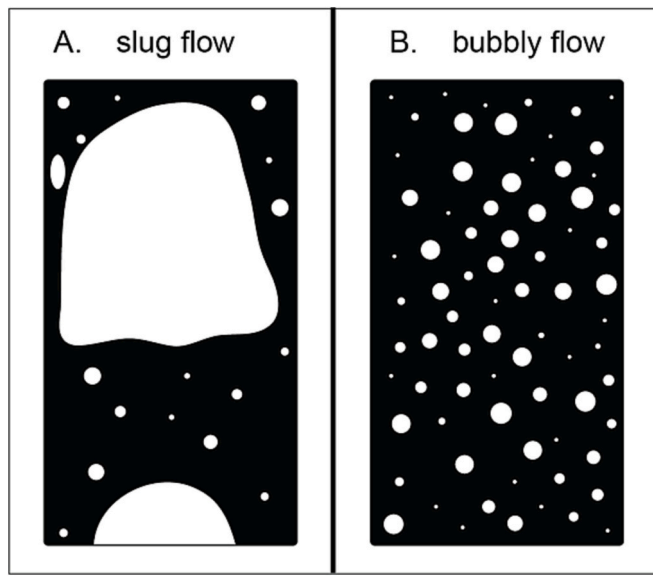


Fig. 1. Schematic sketch of two-phase flow regimes in vertical volcanic conduits, after Gonnermann and Manga (2013) and Pioli et al. (2012). Bubbles are white and black areas represent melt. (A) Slug flow is modeled to drive Strombolian explosions, and (B) coupled bubbly flow is thought to drive Hawaiian fountains (Taddeucci et al., 2015).

both the types of explosions and of their ejecta to delineate precisely the processes driving all contrasting eruption styles. More data sets that cover the full range—including transitional styles—of weak explosive activity, are required to gain a clearer understanding of the factors that promote such diversity in style, and are critical for hazard assessments of future explosive events (Houghton and Gonnermann, 2008). Fissure eruptions are invaluable observational settings to fill data gaps because, unlike single point-source vents, they often offer a diverse range of styles and intensities over small time and distance scales (e.g., Witt et al., 2018; Houghton et al., 2020). In this study, we present observations from the 2018 fissure eruption on Kilauea's lower East Rift Zone (LERZ) that span eruptive styles from Strombolian to Hawaiian.

1.2. Weak explosive activity at the LERZ, Kilauea in 2018

High-definition video footage of the LERZ eruption in May 2018 captured a wide range of mildly explosive eruptive behavior (e.g., Houghton et al., 2020). Magma compositions ranged from basalt to andesite (the latter confined to the western end of Fissure 17 (F17)). The eruption formed a ~ 6.8-km-long array of 24 fissures or fissure segments (Neal et al., 2018; Fig. 2). Due to the dynamic nature of the eruption during its initial month (Fissures 1–15 erupted on timescales of just minutes–hours; Neal et al., 2018), it was impossible to capture footage for all styles of explosive activity at all of the 24 fissures. However, we recorded activity at five fissures (F7, F8, F17, F18, F20; Fig. 2) that was representative of the activity during May 2018.

We recognized both Strombolian explosions over a wide range of explosion frequencies (Fig. 3A, C), and sustained Hawaiian fountains with variable degrees of steadiness (Fig. 3B, D). Strombolian and Hawaiian styles are separated by a wide gap in event duration, following Houghton et al. (2016). The qualifiers 'normal' and 'rapid' for Strombolian activity, and 'steady' and 'unsteady' for Hawaiian fountains, are used here as informal, qualitative terms, and in each case, represent the ends of spectra, rather than distinct eruption regimes. Normal Strombolian activity was restricted to a cluster of andesitic vents at the western end of F17.

2. Methods

2.1. Field recordings

High-definition (4 K; 3840 × 2160 pixel resolution) videos of explosive activity were filmed at different locations using a Sony AX-100 camcorder, operating at 30 frames per second (fps). The camcorder was mounted on a levelled tripod to maximize video stability. The horizontal distance between the camera and the vent was calculated using GPS data taken at the filming sites and vents. Vent locations were obtained during helicopter overflights. The Garmin GPSMAP64s has a published position accuracy of 3 m; the camera-vent distances are thus accurate to ± 6 m.

2.2. Video analysis

The key parameters constrained from field observation and

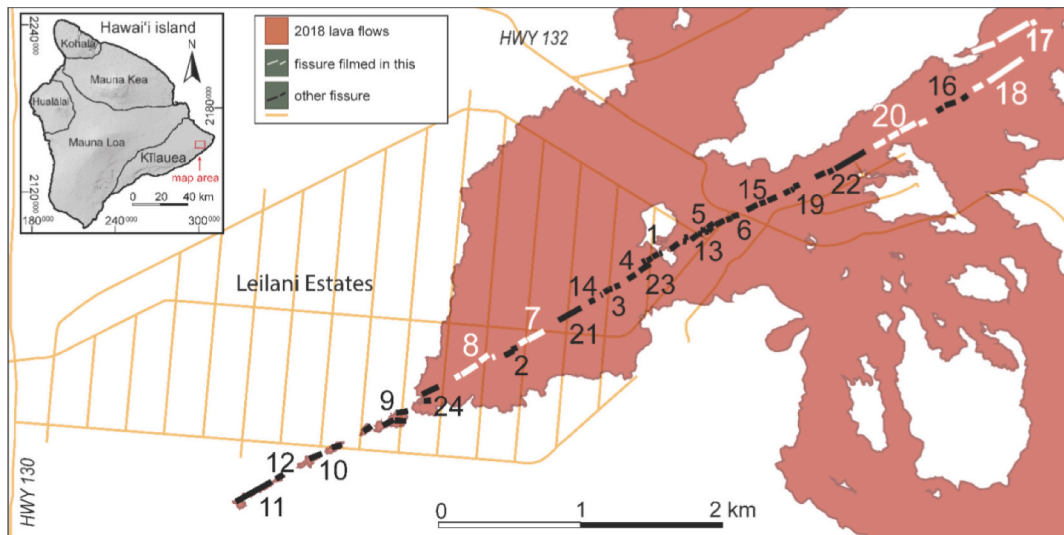


Fig. 2. Map of Kilauea's 2018 lower East Rift Zone fissures. The 24 fissure segments (or clusters of them) were numbered chronologically by the USGS; fissures considered in this study are shown in white. Inset map shows the main map's extent (red rectangle). The base map is a satellite image from DigitalGlobe (2019). Fissure and flow locations were provided by Hawaiian Volcano Observatory staff (2018). (For interpretation of the references to colour in this figure legend, the reader is referred to the web version of this article.)

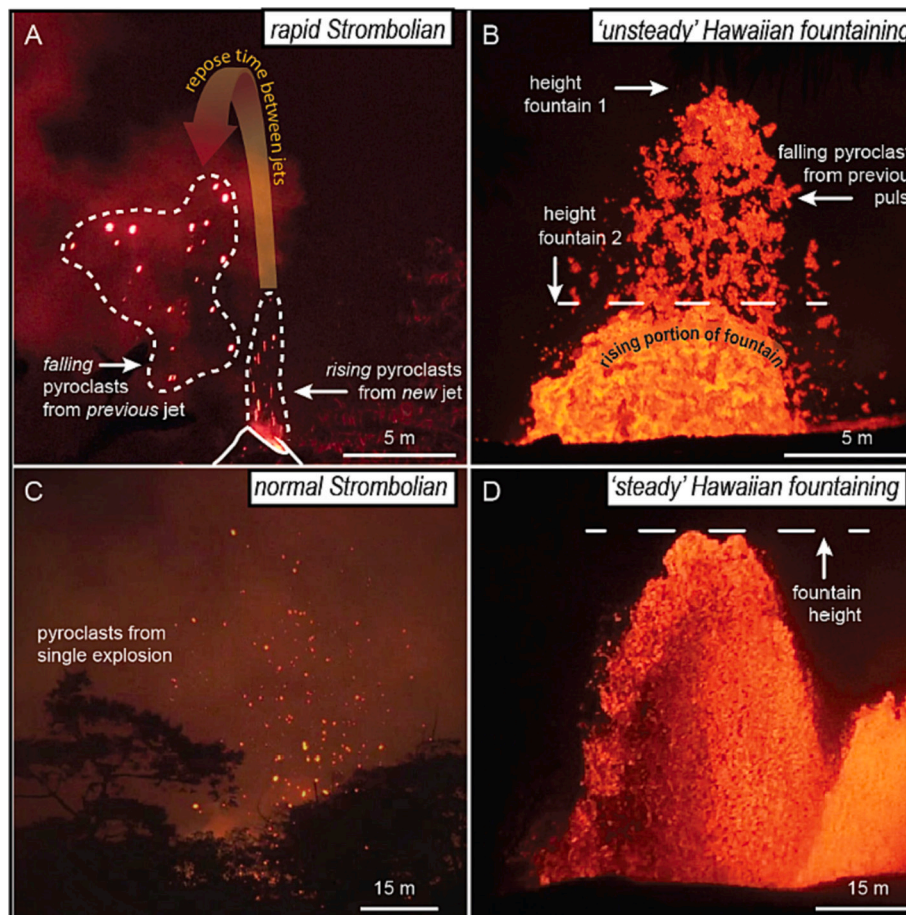


Fig. 3. Single images taken from videos analyzed in this study that exemplify various styles of weak explosive activity. (A) Ejecta from two closely-spaced, weak, rapid Strombolian jets rose to 15–18 m above the vent at F18, at 01:52 on 16 May 2018. (B) A sustained but pulsating Hawaiian fountain from F7 at 02:10 on 27 May 2018. Falling ejecta, associated with the more powerful first pulse, are cooler and hence appear darker; they are positioned above the brighter, hotter, rising ejecta from the next pulse. (C) A weak normal Strombolian explosion from F17 at 02:26 (HST) on 19 May 2018, ejecting decimeter-sized clasts to 60–70 m elevation. (D) An example of steady Hawaiian fountaining behavior from the higher, left-hand F8 fountain at 1951 h on 29 May 2018. Though not discernable when viewing only a single image, the lower, right-hand fountain was more unsteady. (For interpretation of the references to colour in this figure legend, the reader is referred to the web version of this article.)

subsequent analysis of videos are (1) *discrete explosions*: maximum ejecta height, event duration, repose interval, and explosion frequency and (2) *sustained fountains*: the variation in fountain height with time and duration of eruption pulses. To calculate eruption parameters, we first extracted individual frames (images) from our videos. The number of frames per second analyzed was varied according to the frequency of observed activity. Data was sampled at rates ranging from 1 to 30 fps depending on how rapidly activity evolved on screen. For videos that captured Hawaiian fountaining, where the fountain height clearly did not appreciably change on a sub-second scale, analyzing height data at 5 fps or less was sufficient. For videos capturing Strombolian activity, we analyzed at 5 or more fps in order to accurately record the timing of each burst.

Video (image) resolution was converted from pixels to meters by scaling each image by factor r (m/pixels), which considers the horizontal distance between the vent and camcorder d (m), the camcorder's image sensor size B (mm), the pixel resolution p (pixel), and the focal length of the lens f (mm) by

$$r = \frac{d \bullet B}{f \bullet p} \quad (1)$$

(Witt et al., 2018). This approach does not account for parallax, and treats every measured object as if it lies at a single distance d from the camcorder. The scaling factor r was recalculated every time the camera's location or magnification changed.

Ejecta heights for Strombolian explosions are measured from the vent to the maximum elevation attained by incandescent juvenile pyroclasts. Data were acquired manually from the images using MTrackJ, a freeware image analysis plugin for ImageJ (Meijering et al., 2012). Each data set relates to a single, point-source vent (i.e., videos

that capture multiple vents have a data set for each vent). Our categorization of Strombolian explosions excludes examples of very weak spattering activity, which barely reached just above ground level. The duration of an explosion was calculated as the time interval between the appearance of the first and the last pyroclasts. The pre-explosion repose interval was calculated as the time between the end of the previous explosion and the onset of the explosion in question. Frequency was calculated by counting the number of explosions in a video and dividing that by the duration of a video, excluding any time before the first explosion.

Fountain height is defined as the vertical distance between the ground surface and the top of the thermally opaque region. Snapshots of a pyroclastic fountain's mean height were calculated by averaging recorded fountain heights over a span of 60 s at a frequency of 1fps. The degree of unsteadiness of a fountain is expressed as the 'fluctuation', which was also quantified at 1fps over minute-long periods. Fluctuation is herein defined as the mean absolute deviation around the mean of the fountain height over a time interval, expressed as a percentage of the mean fountain height over the same time interval:

$$\text{fluctuation} = \frac{100}{N} \sum_{i=1}^N \frac{|h_i - \bar{h}|}{\bar{h}} \quad (2)$$

where N is the number of measurements of fountain height h , and \bar{h} is the mean fountain height. One minute was chosen as the averaging interval because it is much longer than the time between individual 'pulses' in the fountain height, but much shorter than the life-span of a fountain.

In other words, each minute of video (that captures fountaining activity) has a mean height (based on the average of 60 measurements of fountain height), and a characteristic value for deviation from this value (based on the average of 60 calculations of the difference between

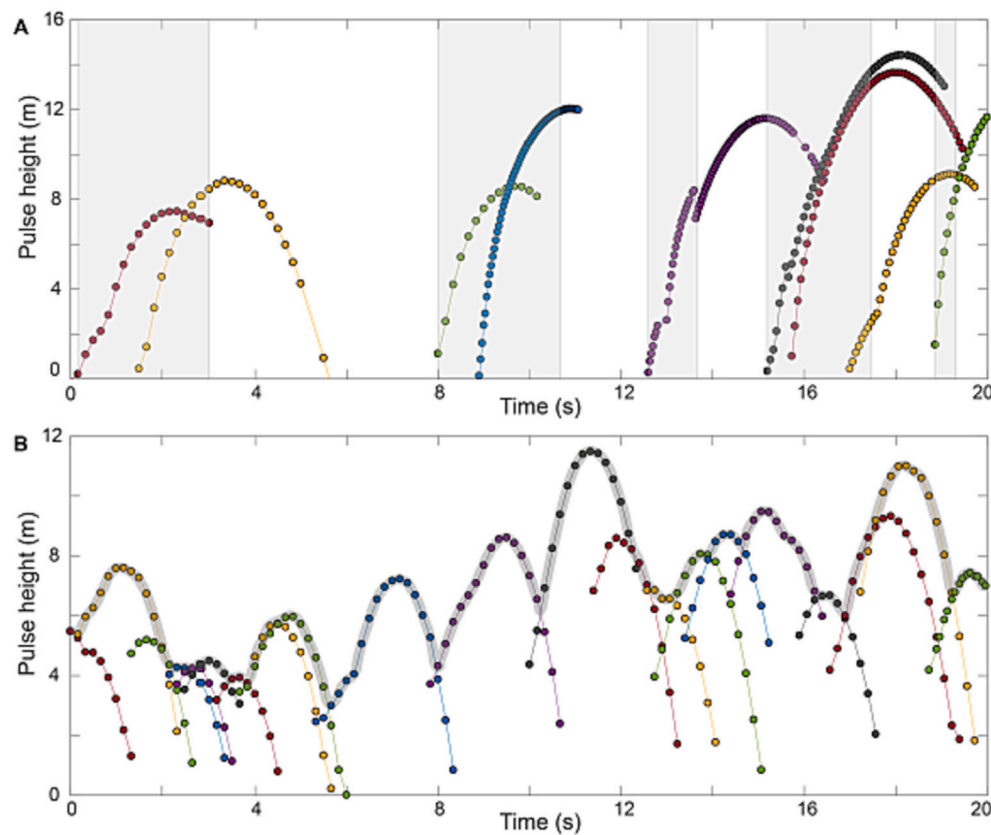


Fig. 4. Pulse height with time for twenty-second-long intervals that are representative of (A) rapid Strombolian and (B) unsteady Hawaiian activity. For each Strombolian event or Hawaiian pulse, we tracked the initial clast and then the highest clast visible in each image. Each curve tracks a single pulse; curves are varied in colour to aid in differentiating closely spaced pulses. (A) Pulse heights during rapid Strombolian activity at F18. Grey boxes outline the start and stop times of individual explosions, during which a continued discharge from the vent was maintained. Data from video 20180516_0152. (B) Plot tracking the evolution of multiple pulses as bubbles rise, burst, and generate pyroclasts (F 20 on 19 May 2018, video 20180519_0331). We tracked the rising gas pocket and then the trajectory of the resulting pyroclasts. The pulses overlapped in both space and time, creating an unsteady Hawaiian fountain whose height is represented by the highest pyroclasts/pulse at any moment (translucent grey line). Pyroclasts were tracked until they became obscured by either vegetation or a subsequent pulse.

instantaneous and mean fountain height). These deviations ($x - \bar{x}$) were converted to percent changes from the average fountain height. Since the fountain height at any point in time could be above or below the mean height, the absolute value of each percent increase or decrease was taken to produce the percent deviation. These percent deviations (60 values per minute) were averaged to create a single value that represents a fountain's fluctuation over each one-minute-long interval. Analyzing each minute of fountaining activity separately helps to capture a more accurate picture of a fountain's steadiness. Otherwise, larger fluctuations would be concealed, as they would have less influence on an average calculated over a longer time period.

The variation in fountain height with time $h(t)$ was also investigated through Fourier analysis, in order to identify and evaluate any

periodicity in height variations. Time series of 1024 height values (one measurement per second) were analyzed using a discrete Fourier transform in MATLAB to determine the frequency distribution of power (power spectral density) using the pwelch function, which implements Welch's power spectral density estimate algorithm (Deardorff et al., 2019).

3. Results

We analyzed 173 discrete explosions at fissures F7, F17, and F18, and 177 min of fountaining behavior at F7, F8 (later stages), and F20. In this section, we present both qualitative observations and quantitative data derived from the videography.

Table 1
Maximum height, duration, and frequency of discrete explosions.

| Video Number | Description | Jet height maxima (m) | | Explosion duration (s) | | Pre-explosion repose interval (s) | | Time analyzed (s) | Number of discrete explosions | Data points per sec | Frequency (events/h) |
|---------------|-------------|-----------------------|----------|------------------------|----------|-----------------------------------|----------|-------------------|-------------------------------|---------------------|----------------------|
| | | mean | σ | mean | σ | mean | Σ | | | | |
| 20180519_0220 | F17, V2 | 32 | 23 | 1.4 | 1.1 | 264.6 | 120.6 | 1260 | 4 | 5 | 11 |
| 20180519_0220 | F17; V3 | 15 | 7 | 1.2 | 0.8 | 265.8 | 153.4 | 1260 | 5 | 5 | 14 |
| 20180519_0220 | F17; V7 | 54 | 34 | 2.0 | 1.4 | 217.0 | 146.3 | 1260 | 6 | 5 | 17 |
| 20180519_0220 | F17; V5 | 35 | 24 | 1.3 | 0.9 | 93.8 | 112.0 | 1260 | 12 | 5 | 34 |
| 20180519_0220 | F17; V6 | 53 | 28 | 2.2 | 1.4 | 101.0 | 111.7 | 1260 | 12 | 5 | 34 |
| 20180519_0220 | F17; V4 | 30 | 22 | 2.0 | 1.6 | 48.3 | 48.6 | 1260 | 21 | 5 | 60 |
| 20180505_1050 | F7, V1 | n.a. | n.a. | 1.2 | 1.1 | 3.4 | 2.9 | 28 | 6 | 30 | 771 |
| 20180516_0152 | F18 | 22 | 10 | 2.9 | 2.6 | 1.0 | 1.0 | 400 | 94 | 6 | 846 |
| 20180505_1050 | F7, V3 | n.a. | n.a. | 0.6 | 0.3 | 3.3 | 0.9 | 28 | 7 | 30 | 900 |
| 20180505_1051 | F7, V3 | n.a. | n.a. | 0.4 | 0.2 | 2.3 | 0.8 | 17 | 6 | 30 | 1270 |

Note: Videos are named using YYYYMMDD_TTTT format, where TTTT represents the start time (HST) of the video in 24-h format. F#; fissure number designated by the USGS. V#; vent number informally assigned by authors in this study.

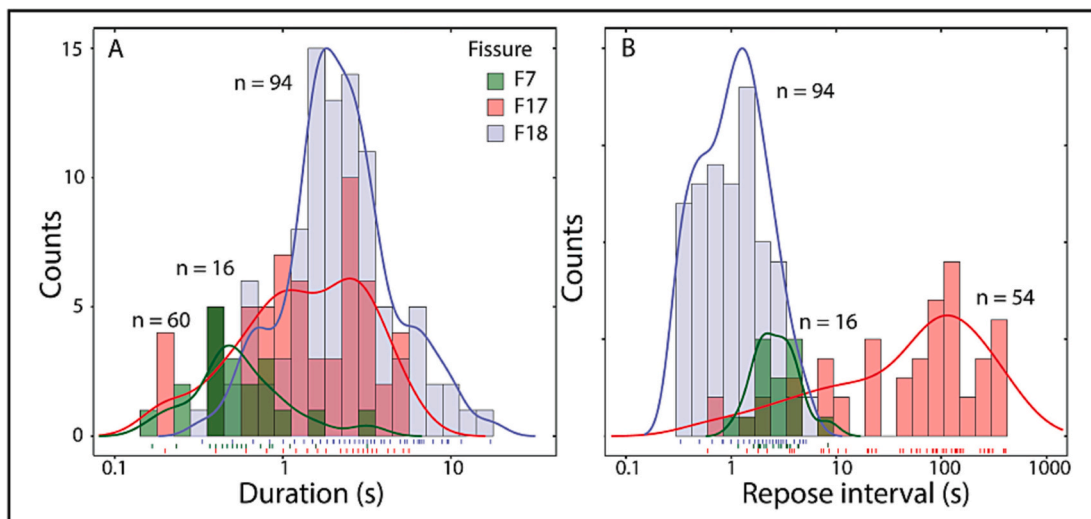


Fig. 5. Histograms of (A) explosion durations, and (B) repose interval between discrete Strombolian explosions at selected vents along fissures 7, 17, and 18. Note logarithmic x-axes. Curves, which are included to guide the eye and aid comparison of the histograms, are data density kernels, scaled by counts for each fissure, computed using the standard ‘density’ function in the R statistical environment.

3.1. Observational results from videography

Much of the recorded activity was not steady. Clearly the Strombolian activity was composed of spaced, distinct explosions of variable duration and with variable repose intervals between explosions. Fig. 4a shows typical time-series data for the maximum pyroclast height for rapid Strombolian activity. Many explosions were themselves composed of multiple pulses. During pulses, clasts often emerge in small clusters, suggesting some even finer, sub-second fluctuations in discharge. In some cases, where lava ponded over a vent and the free surface was visible (e.g., F17, early F8), pulsations could be observed directly. The morphology of the deforming free surface at the onset of each explosive pulse had the form of a bursting gas bubble, and allowed us to estimate bubble diameters on the order of 1–10 m. A single explosion was often the product of multiple gas bubbles bursting in quick succession, each defining a pulse. In cases where the free surface was not visible (either hidden by topography or vegetation) pulsations were still evident in the pattern of release of ejecta (Fig. 4a).

Pulsatory activity was also evident in the ‘unsteady’ Hawaiian fountaining. Fig. 4b shows the results of tracking the highest, visible and upward-moving pyroclast at any time, and continuing to track any such clast past its zenith, and as far through its subsequent fall as possible, until obscured. The unsteady fountain shown in Fig. 4b is composed of multiple, closely-spaced and overlapping pulses. Similar pulses occurred at F8, where we observed the outgassing of large gas pockets in even the most stable fountains. Each pulse creates a sudden transient rise in fountain height.

During Hawaiian fountaining, coherent, unfragmented magma often rose some meters above the walls of the vent, such that large bubbles could be seen bursting through the elevated magma free surface. Above the free surface, the fountain was composed of a mixture of pyroclasts within a continuum gas phase.

3.2. Strombolian explosions

Data for discrete Strombolian explosions are presented in Table 1. The maximum ejecta height was measured for 60 explosions at F17, and 94 at F18. The F18 data were derived from a single point-source vent, whereas the F17 data were derived from six vents spaced linearly along approximately 80 m of fissure. Accurate heights could not be determined for F7, which was filmed from a moving helicopter. The weakest of the recorded explosions reached a maximum height of just 2 m; the most

energetic explosions ejected material out of the camera’s field of view, corresponding to a height greater than ~90 m. The mean maximum height of discrete explosions was 28 m ($\sigma = 19$ m). Values were broadly similar for the two fissures (F17: mean height = 37 m, $\sigma = 26$ m; F18: mean height = 22 m, $\sigma = 10$ m) though note that the F17 mean height would have been higher if the field of view had been large enough to capture the zenith of the highest pyroclasts. Ejecta heights for the different vents at F17 are shown in Fig. A1. The measured heights show a greater range at F17 than at F18, but this does not appear to be an artifact of aggregating data for explosions from multiple vents—explosions from each of four of the six vents analyzed at F17 cover almost the same range as found in the aggregated data (Fig. A1).

The duration of individual explosions was measured for 173 explosions across three fissures (19 at F7, 60 at F17, 94 at F18). The shortest explosion lasted only 0.17 s (5 frames at 30 fps); the longest lasted 17.2 s. The durations span two orders of magnitude, and are approximately normally distributed in logarithmic space (Fig. 5A); consequently, the means and standard deviations are computed in logarithmic space and transformed back to linear space to give dimensional values (note that standard deviations are therefore asymmetrical around the mean; the positive and negative standard deviations given as σ_+ and σ_- respectively; F7: mean duration = 0.55 s, $\sigma_+ = 0.55$ s, $\sigma_- = 0.27$ s; F17: mean duration = 1.3 s, $\sigma_+ = 1.8$ s, $\sigma_- = 0.77$ s; F18: mean duration = 2.2 s, $\sigma_+ = 2.4$ s, $\sigma_- = 1.1$ s). The $+-$ standard deviation bands overlap for all three fissures, indicating that the durations of explosions at all three fissures are similar. The data in Fig. 5 are aggregated across two vents for F7, and six vents for F17 (there was only a single vent at F18); data for each vent are presented in Fig. A2.

The repose intervals before explosions was measured for 163 explosions across three fissures (16 at F7, 54 at F17, 93 at F18). The shortest repose interval was only 0.33 s (11 frames at 30 fps); the longest lasted 411 s. The durations span three orders of magnitude; durations for F7 and F18 are approximately normally distributed in logarithmic space (Fig. 5b). The distribution for F17 is more irregular and skewed towards longer intervals (F7: mean duration = 2.7 s, $\sigma_+ = 1.7$ s, $\sigma_- = 1.0$ s; F17: mean duration = 44 s; F18: mean duration = 1.0 s, $\sigma_+ = 1.1$ s, $\sigma_- = 0.54$ s; note that the skewing of the F17 data preclude determination of meaningful standard deviation). The repose interval is similar for fissures 7 and 18, but more than an order of magnitude longer for fissure 17. This may be explained, in part, by the fact that interval data for F17 are aggregated across six vents; this is discussed later in Section 4.

Explosion frequency ranged from 11 to 1270 events per hour. One

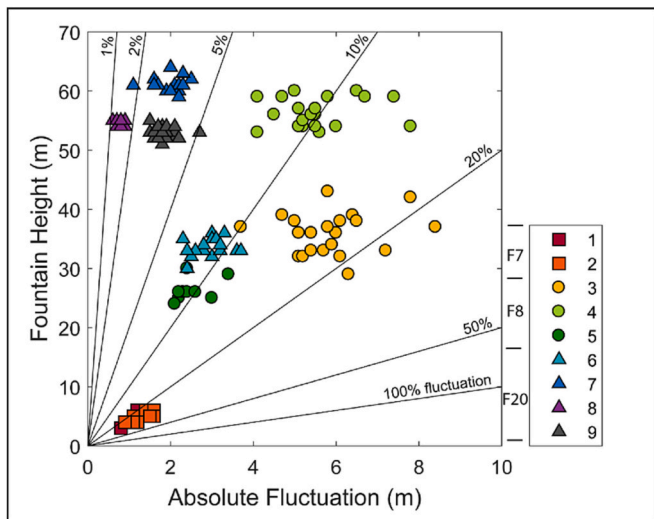


Fig. 6. Plot of mean fountain height vs. absolute fluctuation for 198 min of fountaining activity at F7 (squares), F8 (triangles), and F20 (circles). Iso-lines are shown for fluctuation as a percentage of mean fountain height. Data sets '1–9' are numbered in chronological order. If two video recordings filmed the same fountain, and the hiatus between the two recordings was <1.5 h, the data were merged into a single data set. The time, location, and other metadata for the video recordings that underpin the nine data sets are given in Table A1.

pattern of Strombolian explosions on the LERZ in 2018, as seen at six andesitic vents on F17 on 19 May, was explosion frequencies ranging from one event per minute up to one event every 5–6 min (Table 1). Four other analyzed videos display much higher eruption frequencies, ranging from 13 to 21 events per minute, which corresponds to a situation where the repose time and the duration of the events have converged. In general, in 2018, very high explosion frequencies typified the Strombolian activity.

3.3. Hawaiian fountaining

Data for nine separate periods of Hawaiian fountaining are presented in Fig. 6; mean heights and fluctuations are recorded over multiple one-minute intervals as described in Section 2.2. Mean heights and

fluctuation values of fountains ranged from 3 to 64 m, and 1 to 32%, respectively. No pauses were observed, but there were short periods when the fissure was not being directly monitored, in which there may have been pauses. In the extreme, it is possible that discharge at F8 was continuous for 60 days (from 28 May to 26 July).

Data from two periods of fountaining—typical of steady and unsteady behavior respectively—were selected for Fourier analysis following the procedure outlined in Section 2 that allows us to identify periodicity in height variations in the two datasets. The raw $h(t)$ data and results of the Fourier analysis are presented in Fig. 7. Note that the two datasets presented in Fig. 7A correspond to the light blue triangles (unsteady) and dark blue triangles (steady) shown in Fig. 6. As expected, the power spectral density is higher in magnitude for the unsteady fountain (note different axis scales for the two datasets). The unsteady fountain also shows noteworthy spikes in the power spectral density at periods of around 7 s and 200 s. Spikes in the power spectral density for the steady fountain are less pronounced.

3.4. Data quality

A major strength of the data presented here is their high temporal and spatial resolution, which allow more detailed analysis of fountaining activity than has been possible for previous eruptions in Hawai'i. A limitation is that the video footage only captures a small fraction of the activity over the duration of the eruption, because footage was collected opportunistically, by field crews whose principal task was assessing public safety. Nonetheless, qualitative observations were made every day and they indicate that the events we describe here are fully representative of the diversity of the explosive activity during the eruption. A further complication is that the Strombolian dataset is inherently biased towards events that occur more frequently. This is reflected, for example, in the different number of data points for explosions from the different fissures (Fig. 4 and Table 1). Consequently, the statistics presented in Table 1 are more robust for those vents with more frequent explosions. There is also a relatively continuous spread in values for Hawaiian fountain fluctuation, but not for height (Fig. 6). We suspect this is an artifact of incomplete sampling. With more data, the apparent gaps in the height data may thus disappear.

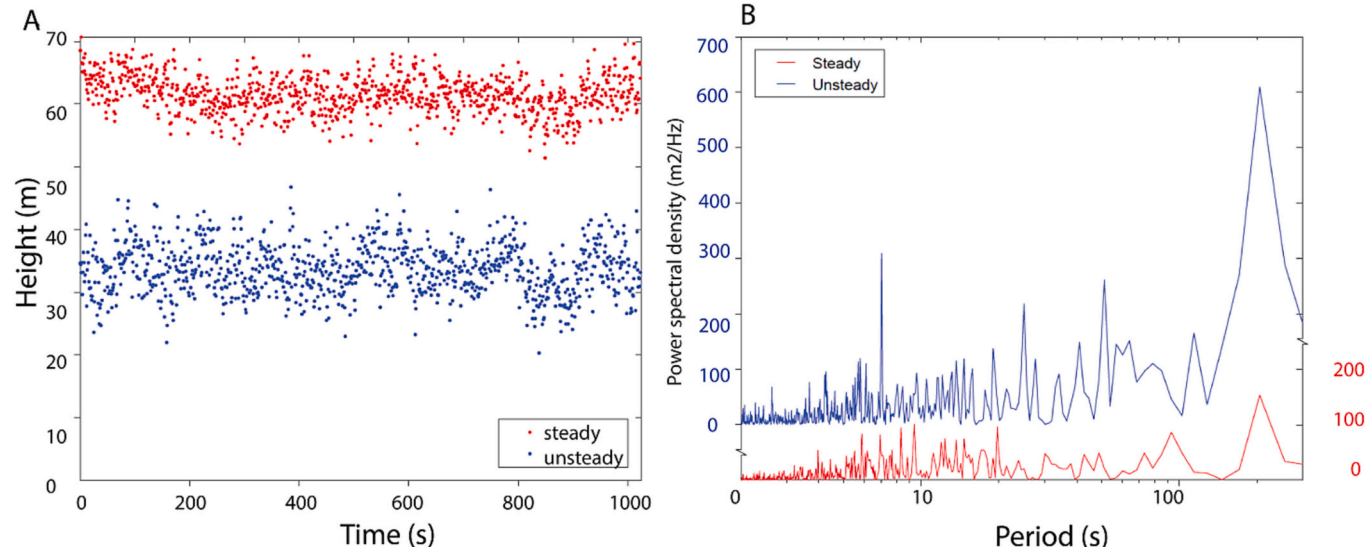


Fig. 7. (A) Time series for fountain height, sampled at 1 Hz, for a typical steady and a typical unsteady Hawaiian fountain. These were the two main fountains located at fissure 8 on 29 May 2018 (video 20180529_1951, Table A1). (B) Power spectral density computed from data in (a) using Fourier analysis (Section 2). Note that y-axes for the two spectra are offset to aid interpretation.

4. Interpretation and discussion

4.1. Strombolian activity

Observations of the magma-free surface, for example, at F7 and F17 (Section 3.1), indicate that Strombolian activity was driven by the bursting of pockets of mechanically decoupled gas bubbles rising independently through slowly ascending magma, consistent with the prevailing conceptual models (Blackburn et al., 1976; Parfitt, 2004; Taddeucci et al., 2015). The observations and analysis of time-series data for ejecta heights (Fig. 4a) provide clear evidence that a single explosion may be driven by the bursting of multiple bubbles, which are closely spaced in time, and form a single gas pocket.

The cross-sectional diameters of gas pockets are $\sim 1\text{--}5$ m, estimated from the deformation of the magma free surface, and are consistent with estimates from computational models of bubble size at Stromboli and elsewhere (James et al., 2013). These numbers are also consistent with values assumed for the conduit width in numerical models of basaltic fissure eruptions on Kilauea's ERZ and elsewhere (Wilson and Head III, 1981; Wilson and Head, 1988) and similar to the width of surface fissures on Kilauea (e.g., Parcheta et al., 2015) and shallow feeder dikes in Iceland and in the southwestern U.S. (Reynolds et al., 2016; Keating et al., 2008).

Our data show that explosion durations are nearly identical for both normal and rapid Strombolian events (Fig. 5A). We therefore infer that the nature of the mechanism driving explosions is the same (rising, bursting gas pockets) for all types of Strombolian activity we saw. The narrow range of durations is also consistent with a stable, relatively organized conduit, with relatively consistent volumes for the bursting gas pockets.

The explosion frequency—linked to repose interval—varies by 2 orders of magnitude in time and space (Table 1). The means of the repose intervals are clearly different for different fissures (Fig. 5B); however, collectively the repose intervals form a spectrum (Fig. A3). The principal variable is the repose interval (or frequency) of explosions. That is, there is no fundamental difference between the mechanisms of rapid and normal explosions.

Rose reflects the time necessary to form a sufficiently large gas pocket to rise freely through the surrounding melt. For a given gas flux, a dispersed series of vents will lead to longer repose intervals than a system where the gas flux is focused into a single vent. The F18 data came from one vent and the F17 data from six vents spaced over 80 m. The F18 data were predictably more tightly grouped, reflecting the simpler vent and conduit geometry. For F17, the wider spread of data indicates that individual vents behaved somewhat independently of each other, reflecting a more complex two-phase flow and a more varied range of vent and conduit geometries.

Considering the large variation of Strombolian explosion frequencies, and assuming most of the gas pockets are similar in size (based on the similar durations of explosions) and with similar degrees of bubble overpressure, then we can assume, to a first order that the total gas budget increases with the frequency of explosions. The gas flux will be higher therefore during rapid Strombolian activity than it would be during normal Strombolian activity. A limitation on our interpretation is the relatively small number of vents and fissures for which we have quantitative data.

Normal Strombolian activity on Kilauea's LERZ in 2018 had a similar frequency to such activity observed at Stromboli volcano. However, the only studies at Stromboli that can be used to make direct comparisons to our normal Strombolian data are Patrick et al. (2007) and Salvatore et al. (2018) because they also present data from single vent sources. Patrick et al. (2007) recorded 344 events in 2001–2004 with explosion frequencies of 3.8–4 events per hour. Explosion durations during their observation period ranged from 6 to 41 s, on average 15 s. Salvatore et al. (2018) report a total of 4785 explosions from 8 source vents. Data were collected over one 3-day interval each year, from 2005 to 2009.

Averaged over the total collection time (45 days) explosion frequencies for single vents ranged from 0.4 to 4.2 events per hour. Mean event durations ranged from 3 to 13 s, with a total range of values of 1 to 26 s. Several other studies at Stromboli present explosion frequency data averaged from explosions at multiple vents (e.g., Harris and Ripepe, 2007; Ripepe et al., 2008; Taddeucci et al., 2013; Gaudin et al., 2017) and the data give predictably higher results in terms of explosion frequency (i.e., frequency values ranging from 5 to 27 events per hour) comparable to all-vent numbers given in Salvatore et al. (2018). No data on the length of repose intervals were reported in any of these studies.

Rapid Strombolian activity on the LERZ in 2018 can be compared to studies of similar activity from single vents at Etna (Italy) and Villarrica (Chile). At Villarrica, Gurioli et al. (2008) recorded 254 events in 78.5 min, giving a frequency of 194 events per hour. The average duration of these events was 0.7 s (with a standard deviation of 0.5 s). The heights of ejecta from these explosions ranged from 1 to 28 m, with an average of 10 m and a standard deviation of 7 m. Pering et al. (2015) recorded 195 explosions in 27 min at Etna, giving a frequency of 433 events per hour. These events were all <4 s long, with repose intervals lasting between 1 and 46 s (mode of 4 s, median of 5 s). Spina et al. (2017) recorded 11 and 23 events respectively over 28 s at Etna in 2014, equivalent to frequencies of 1414 and 2957 events per hour. The frequency of rapid Strombolian activity on the LERZ (771–1270 events/h), is similar to these studies, which are the only published examples with quantitative frequency data for this style.

4.2. Hawaiian activity

All fountains are unsteady to some extent, and there is a continuous range of unsteadiness as seen in the fluctuation data (Fig. 6). The steadiest fountain (F8 on 29 May) has a fluctuation value of just 1.1%, but this degree of steadiness was rare. There is no apparent correlation between fluctuation and mean fountain height (i.e., for any given height, some fountains are extremely stable whereas others show considerable fluctuation; Fig. 6). We therefore infer that two different processes are responsible for fountain height and fountain unsteadiness. Strombolian and unsteady Hawaiian events show similar patterns of pulsation (Fig. 4) so we infer that the process causing pulsations in the fountains is the same as the process driving discrete Strombolian explosions (i.e., the arrival and bursting of decoupled gas pockets). Our observations exclude the possibility that the 2018 fountains were formed by annular flow of magma in the conduit, as has been suggested by some workers (e.g. Pioli et al., 2012).

We suggest that the degree of a fountain's unsteadiness is linked to the frequency of arrival of decoupled gas pockets (Fig. 4b), which in turn, reflects the portion of the flux of gas that is ascending rapidly through the conduit. This was directly observed at F8, where each large gas pocket created a sudden rise in fountain height. Steady fountaining behavior seems only possible where escape of large gas pockets plays an insignificant role, relative to the steady expansion of the population of smaller bubbles that are always present and are mechanically coupled to the melt phase during ascent and eruption.

We speculate that the time-averaged height of the fountain is controlled by the exit velocity of the melt and coupled bubbles. During the intervals between pulses, the magma's gas mass fraction is provided by the gas in small bubbles in the magma that have escaped being absorbed by the preceding large, decoupled gas pocket. During the pulses, the magma's gas mass fraction consists of small bubbles like those just mentioned plus the gas pocket driving the pulse. Thus, during a pulse, the effective gas mass fraction of the erupting magma is greater. Therefore, we infer that there is a spectrum of Hawaiian fountaining activity, the diversity of which is influenced by (1) frequency of decoupled gas pockets, and (2) flux of melt and coupled bubbles—i.e. 'steady' and 'unsteady' are relative terms, and there is no dichotomy.

Fourier analysis (Fig. 7b) shows peaks in power spectral density around 7 s for the unsteady fountain, which is in the middle of the range

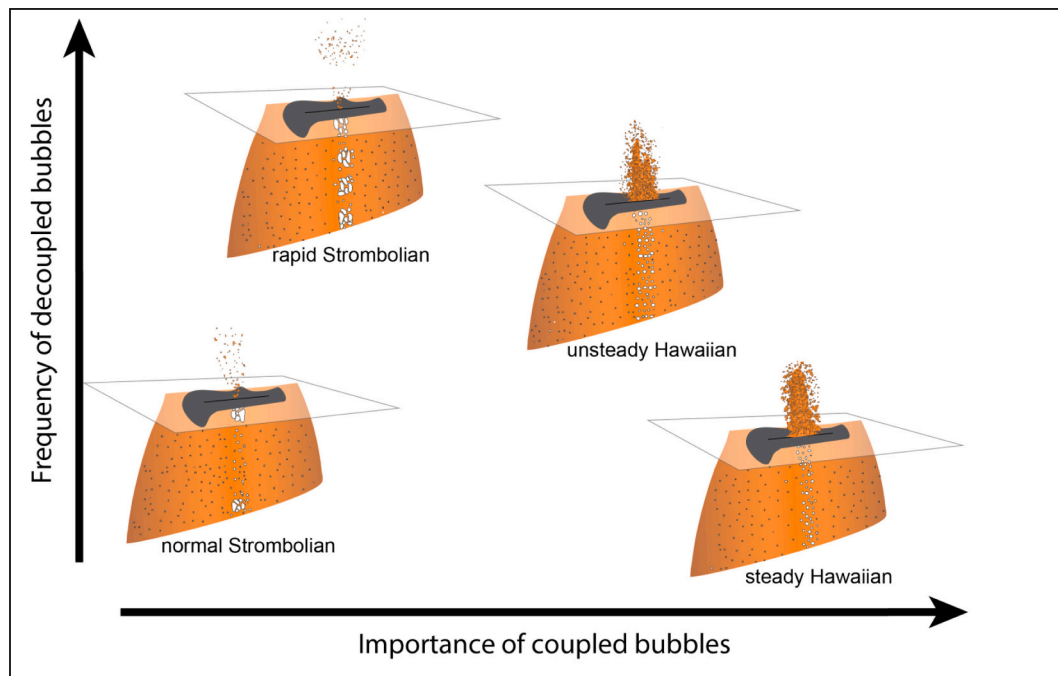


Fig. 8. Conceptual model for the gas–magma organization in the conduit that gives rise to the spectrum of styles of activity observed (see Fig. 3).

of repose intervals for Strombolian pulsations (Fig. 5b). A longer-term fluctuation in fountaining vigor at F8 on timescales of 5–10 min was recognized by Patrick et al. (2019) and correlated with variation in the efficiency of outgassing. In contrast, fluctuations in eruption rate on longer timescales (1–2 days) appear to relate to external influences—to pulsations in conduit flow linked to pressurization due to small summit collapses (Patrick et al., 2019).

The eruptive behavior at F8 from late May to late July is atypical among 20th-century Hawaiian fountains in terms of the extended duration(s). The main fountaining episode at F8 in 2018 lasted for perhaps two months (Patrick et al., 2019). Episodes during previous eruptions at Kilauea were much shorter lived (e.g., Richter et al., 1970; Swanson et al., 1976; Wolfe et al., 1988). The average episode duration for the 1959 Kilauea Iki eruption was 20.3 h (Richter et al., 1970). The average duration for the fountaining episodes in 1969 of the Mauna Ulu eruption is 18 h (Swanson et al., 1976). In the last major fountaining eruption, at Pu'u 'O'o from 1983 to 1986, episodes ranged in duration from 5 min to 16 h (Wolfe et al., 1988). The average duration (for the first 48 episodes of the Pu'u 'O'o eruption) is 43 h (Heliker and Mattox, 2003). The position of the F8 vent low on the East Rift Zone (40 km from the summit) and the well-established conduit-vent system were probably major factors that contributed to the long duration of the last episode at F8. Many of the early 2018 episodes were short lived because the shallow conduit was not well established early in the eruption and the discharged magma was relatively viscous (Soldati et al., 2021).

4.3. A unified model for Strombolian and Hawaiian activity

Cases where the contrasting eruption styles occurred in extremely close proximity and overlapping in time during the 2018 LERZ eruption suggest that the style was determined by processes in the shallowest part of the conduit. The classical understanding of Strombolian vs. Hawaiian activity is that the distinction arises from two fundamentally different types of bubble size distributions and sharp contrasts in bubbly flow in the conduit. In these models, a population of smaller (cm to sub-mm sized) bubbles, coupled to the melt, drives Hawaiian behavior, whereas larger (m-sized) decoupled bubbles that rise independently through the melt drive Strombolian behavior. However, field

observations of ejecta from all four 2018 eruption styles show that they all contained a population of abundant small bubbles that must have been coupled to the melt at the time of fragmentation. The 2018 videos also show that, in every case, large, mechanically decoupled bubbles burst with varying frequency through the free surface. This suggests that the key difference among the eruptive styles in 2018 is the unequal partitioning of available exsolved gas between these two co-existing bubble sub-populations (Fig. 4). Thus, the contrast between normal Strombolian and Hawaiian behavior is due to the higher ratio of small, coupled bubbles to large, decoupled bubbles. Contrasts in the nature of magma outgassing at other frequently active basaltic volcanoes has been interpreted as due to several underlying influences, e.g., magma composition, changes in gas pocket volume with respect to the conduit diameter, and the thickness of a higher viscosity magma layer immediately below the free surface (as shown for Strombolian styles by Gurioli et al., 2014; Del Bello et al., 2015; Capponi et al., 2016, and Gaudin et al., 2017). At least the first two of these factors also influenced eruptive activity on the LERZ in 2018. Magma composition has a major influence on the patterns of outgassing and hence the style of activity, particularly at F17 (i.e., Strombolian versus Hawaiian eruptions) and for modulating frequency of Strombolian explosions. The least frequent Strombolian explosions only occurred at western F17, which is the only vent cluster that erupted cooler magma of andesitic composition. Composition is important because of the influence on viscosity—it is likely to have produced a 2 order-of magnitude-higher viscosity at the western end of F17 compared with the fountaining at F8 (Soldati et al., 2021). Field parties observed an increase in the total flux of decoupled gas during the later phase of the eruption, and this coincided with focusing of eruptive activity on a single stable fissure (Patrick et al., 2019).

However, the dominant influence in determining impulsive transient explosions vs. emergent sustained fountaining remains the size distribution of the bubble population in the erupting magma (Fig. 8). We propose that fountain height increases as the fraction of coupled bubbles increases (x-axis) because a higher total gas abundance gives rise to greater expansion of the ascending magma in the shallow plumbing system, and thus promotes higher exit velocities. We propose that unsteadiness in activity (whether Strombolian or Hawaiian) increases with

the size and frequency of decoupled bubbles or gas pockets that rise through the magma, with pulses in activity corresponding to the arrival/bursting of decoupled bubbles. In this conceptual model, the spectrum of Strombolian and Hawaiian activity results from the interplay between these two independent parameters. We propose that this model (Fig. 8) is more broadly applicable to Strombolian and Hawaiian volcanism globally.

5. Conclusion

Fluctuations in the height of Hawaiian fountains and the frequency of Strombolian explosions have a similar explanation, namely the frequency of bursting of large gas pockets. These styles are similar phenomenologically—there is a full spectrum of explosive behavior from normal Strombolian explosions to steady Hawaiian fountaining—reflecting the variable proportions of coupled and decoupled bubbles.

A simplistic binary model for Strombolian and Hawaiian eruptive behavior is strictly not correct for Kīlauea. Instead, these two ‘end-member’ styles form a spectrum that is governed by the behavior of the exsolved gas phase with respect to the melt in the conduit.

The data sets presented here use timing and/or height fluctuation of explosive phenomena rather than mass eruption rate to explain and interpret eruption styles. This approach has practical value for response teams that monitor eruptions because mass flux, the basis for most classifications of eruptive style (e.g. Walker, 1973; Pyle, 2015), is one of the most difficult parameters to constrain during (and even after) an eruption. This will allow for better communication and description of the unfolding of events both during and after an eruption.

Declaration of Competing Interest

The authors declare that they have no known competing financial interests or personal relationships that could have appeared to influence the work reported in this paper.

Data availability

Data will be made available on request.

Acknowledgements

This work was financially supported by the National Science Foundation (grants numbers EAR-1829188 and EAR-2119838) to Houghton. The authors are grateful to the Hawaiian Volcanoes Observatory staff members and collaborators for the opportunity to participate as part of the eruption response team. We also thank C. M. Tisdale, S. Borotau, and C. MacDonald for assistance with ImageJ processing. This manuscript was greatly improved thanks to helpful and prompt feedback from Jacopo Taddeucci as well as four anonymous journal reviewers, and editors Jim Gardner and Kelly Russell.

Appendix A. Supplementary data

Supplementary data to this article can be found online at <https://doi.org/10.1016/j.jvolgeores.2023.107754>.

References

Andronico, D., Cannata, A., Di Grazia, G., Ferrari, F., 2021. The 1986–2021 paroxysmal episodes at the summit craters of Mt. Etna: Insights into volcano dynamics and hazard. *Earth Sci. Rev.* 220, 103686.

Blackburn, E.A., Wilson, L., Sparks, R.J., 1976. Mechanisms and dynamics of strombolian activity. *J. Geol. Soc.* 132 (4), 429–440.

Calvari, S., Salerno, G.G., Spampinato, L., Gouhier, M., La Spina, A., Pecora, E., Harris, A. J.L., Labazuy, P., Biale, E., Boschi, E., 2011. An unloading foam model to constrain Etna's 11–13 January 2011 lava fountaining episode. *J. Geophys. Res.* 116, B11207. <https://doi.org/10.1029/2011JB008407>.

Calvari, S., Cannavò, F., Bonaccorso, A., Spampinato, L., Pellegrino, A.G., 2018. Paroxysmal explosions, lava fountains and ash plumes at Etna volcano: eruptive processes and hazard implication. *Front. Earth Sci.* 6, 107. <https://doi.org/10.3389/feart.2018.00107>.

Capponi, A., James, M.R., Lane, S.J., 2016. Gas slug ascent in a stratified magma: Implications of flow organization and instability for Strombolian eruption dynamics. *Earth Planet. Sci. Lett.* 435, 159–170. <https://doi.org/10.1016/j.epsl.2015.12.028>.

Deardorff, N., Booth, A., Cashman, K., 2019. Remote characterization of dominant wavelengths from surface folding on lava flows using lidar and discrete Fourier Transform analyses. *Geochem. Geophys. Geosyst.* 20 (8), 3952–3970.

Del Bello, E., Lane, S.J., James, M.R., Llewellyn, E.W., Taddeucci, J., Scarlato, P., et al., 2015. Viscous plugging can enhance and modulate explosivity of strombolian eruptions. *Earth Planet. Sci. Lett.* 423, 210–218. <https://doi.org/10.1016/j.epsl.2015.04.034>.

DigitalGlobe, 2019. LERZ Basemap. NextView License.

Gaudin, D., Taddeucci, J., Scarlato, P., et al., 2017. Integrating puffing and explosions in a general scheme for Strombolian-style activity. *J. Geophys. Res. Solid Earth.* <https://doi.org/10.1002/2016JB013707>.

Gonnermann, H.M., Manga, M., 2013. Dynamics of magma ascent in the volcanic conduit. In: Fagents, S.A., Gregg, T.K.P., Lopes, R.M.C. (Eds.), *Modeling Volcanic Processes, the Physics and Mathematics of Volcanism*. Cambridge University Press, Cambridge.

Gurioli, L., Harris, A.J.L., Houghton, B.F., et al., 2008. Textural and geophysical characterization of explosive basaltic activity at Villarrica volcano. *J. Geophys. Res.* 113 <https://doi.org/10.1029/2007JB005328>.

Gurioli, L., Colo, L., Bollasina, A.J., et al., 2014. Dynamics of Strombolian explosions: inferences from field and laboratory studies of erupted bombs from Stromboli volcano. *J. Geophys. Res. Solid Earth* 119, 319–345. <https://doi.org/10.1002/2013JB010355>.

Harris, A., Ripepe, M., 2007. Temperature and dynamics of degassing at Stromboli. *J. Geophys. Res.* 112, B03205. <https://doi.org/10.1029/2006JB004393>.

Hawaiian Volcano Observatory staff, 2018. Preliminary map of the 2018 lower East Rift Zone eruption of Kīlauea Volcano, Island of Hawai‘i. U.S. Geological Survey. <https://doi.org/10.5066/P9940GY8>.

Heliker, C., Mattox, T.N., 2003. The First Two Decades of the Pu ‘u ‘O‘ō-Kiapaianaha. US Geological Survey Professional Paper, 1676, p. 1.

Houghton, B.F., Gonnermann, H.M., 2008. Basaltic explosive volcanism: Constraints from deposits and models. *Chem. Erde Geochem.* 68, 117–140. <https://doi.org/10.1016/j.chemer.2008.04.002>.

Houghton, B.F., Taddeucci, J., Andronico, D., et al., 2016. Stronger or longer: Discriminating between Hawaiian and Strombolian eruption styles. *Geology* 44, 163–166. <https://doi.org/10.1130/G37423.1>.

Houghton, B.F., Tisdale, C.M., Llewellyn, E.W., Taddeucci, J., Orr, T.R., Walker, B.H., Patrick, M.R., 2020. The birth of a Hawaiian fissure eruption. *J. Geophys. Res. Solid Earth* 126, e2020JB020903. <https://doi.org/10.1029/2020JB020903>.

James, M.R., Lane, S.J., Houghton, B.F., 2013. Unsteady explosive activity: Strombolian eruptions. In: Fagents, S.A., Tracy, K.P.G., Rosaly, M.C.L. (Eds.), *Modeling Volcanic Processes: The Physics and Mathematics of Volcanism*. Cambridge University Press, England, pp. 107–127.

Jaupart, C., Vergniolle, S., 1988. Laboratory models of Hawaiian and Strombolian eruptions. *Nature* 331, 58–60.

Keating, G.N., Valentine, G.A., Krier, D.J., Perry, F.V., 2008. Shallow plumbing systems for small-volume basaltic volcanoes. *Bull. Volcanol.* 70 (5), 563–582.

Macdonald, G.A., 1972. Volcanoes. Prentice-Hall, Inc, Englewood Cliffs, New Jersey, 510 p.

Meijering, E., Dzyubachyk, O., Smal, I., 2012. Methods for cell and particle tracking. In: *Methods in Enzymology*. Elsevier, pp. 183–200.

Mercalli, G., 1881. Natura nelle eruzioni dello Stromboli ed in generale dell'attività sismico-vulcanica delle Isole Eolie. *Atti Soc. Ital. Sci. Nat.* 24, 105–134.

Neal, C.A., Brantley, S.R., Antolik, L., et al., 2018. The 2018 rift eruption and summit collapse of Kīlauea Volcano. *Science* 363, 367–374. <https://doi.org/10.1126/science.aav7046>.

Parcheta, C.E., Fagents, S.A., Swanson, D.A., Houghton, B.F., Erickson, T., 2015. Hawaiian fissure fountains: Quantifying vent and shallow conduit geometry, Episode 1 of the 1969–1974 Mauna Ulu eruption. In: *Hawaiian Volcanoes, From Source to Surface*. AGU Monograph Series, pp. 369–392.

Parfitt, E.A., 2004. A discussion of the mechanisms of explosive basaltic eruptions. *J. Volcanol. Geotherm. Res.* 134 (1–2), 77–107.

Patrick, M.R., Harris, A.J.L., Ripepe, M., Dehn, J., Rothery, D.A., Calvari, S., 2007. Strombolian explosive styles and source conditions: Insights from thermal (FLIR) video. *Bull. Volcanol.* 69, 769–784. <https://doi.org/10.1007/s00445-006-0107-0>.

Patrick, M.R., Dietterich, H.R., Lyons, J.J., Diefenbach, A.K., Parcheta, C., Anderson, K. R., Kauahikaua, J.P., 2019. Cyclic lava effusion during the 2018 eruption of Kīlauea Volcano. *Science* 366 (6470).

Pering, T.D., Tamburello, G., McGonigle, A.J.S., et al., 2015. Dynamics of mild Strombolian activity on Mt. Etna. *J. Volcanol. Geotherm. Res.* 300, 103–111. <https://doi.org/10.1016/j.jvolgeores.2014.12.013>.

Pioli, L., Bonadonna, C., Azzopardi, B.J., Phillips, J.C., Ripepe, A.M., 2012. Experimental constraints on the outgassing dynamics of basaltic magmas. *J. Geophys. Res. Solid Earth* 117 (B3).

Pyle, D.M., 2015. Sizes of volcanic eruptions. In: Sigurdsson, H., Houghton, B., McNutt, S., Rymer, H., Stix, J. (Eds.), *The Encyclopedia of Volcanoes*, 2nd edn. Academic Press, San Diego, pp. 257–264.

Reynolds, P., Brown, R.J., Thordarson, T., Llewellyn, E.W., 2016. The architecture and shallow conduits of Laki-type pyroclastic cones: insights into a basaltic fissure eruption. *Bull. Volcanol.* 78 (5), 36.

Richter, D.H., Eaton, J.P., Murata, K.J., Ault, W.U., Krivoy, H.L., 1970. Chronological Narrative of the 1959–60 Eruption of Kilauea Volcano, Hawaii USGS Professional Paper 537-E.

Ripepe, M., Donne, D.D., Harris, A., Marchetti, E., Olivieri, G., 2008. Dynamics of Strombolian activity. *GMS* 182, 39–48.

Salvatore, V., Silleni, A., Cornelì, D., Taddeucci, J., Palladino, D.M., Sottili, G., Cristaldi, A., 2018. Parameterizing multi-vent activity at Stromboli Volcano (Aeolian Islands, Italy). *Bull. Volcanol.* 80, 64.

Soldati, A., Houghton, B.F., Dingwell, D.B., 2021. A lower bound on the rheological evolution of magmatic liquids during the 2018 Kilauea eruption. *Chem. Geol.* 576, 120272. <https://doi.org/10.1016/j.chemgeo.2021.120272>.

Spina, L., Taddeucci, J., Cannata, A., et al., 2017. Time-series analysis of fissure-fed multi-vent activity: a snapshot from the July 2014 eruption of Etna volcano (Italy). *Bull. Volcanol.* 79, 51. <https://doi.org/10.1007/s00445-017-1132-x>.

Swanson, D.A., Jackson, D.B., Koyanagi, R.Y., Wright, T.L., 1976. The February 1969 East Rift Eruption of Kilauea Volcano. Hawaii.

Taddeucci, J., Palladino, D.M., Sottili, G., Bernini, D., Andronico, D., Cristaldi, A., 2013. Linked frequency and intensity of persistent volcanic activity at Stromboli (Italy). *Geophys. Res. Lett.* 40, 3384–3388.

Taddeucci, J., Edmonds, M., Houghton, B.F., James, M.R., Vergniolle, S., 2015. Hawaiian and Strombolian eruptions. In: Sigurdsson, H., Houghton, B., McNutt, S., Rymer, H., Stix, J. (Eds.), *The Encyclopedia of Volcanoes*, 2nd edn. Academic Press, San Diego, pp. 485–505. <https://doi.org/10.1016/B978-0-12-385938-9.00027-4>.

Walker, G.P., 1973. Explosive volcanic eruptions—a new classification scheme. *Geol. Rundsch.* 62, 431–446.

Wilson, L., Head, J.W., 1988. Nature of local magma storage zones and geometry of conduit systems below basaltic eruption sites: Pu'u O'o, Kilauea East Rift, Hawaii, example. *J. Geophys. Res. Solid Earth* 93 (B12), 14785–14792.

Wilson, L., Head III, J.W., 1981. Ascent and eruption of basaltic magma on the Earth and Moon. *J. Geophys. Res. Solid Earth* 86 (B4), 2971–3001.

Witt, T., et al., 2018. The Relationship between Lava Fountaining and Vent Morphology for the 2014–2015 Holuhraun Eruption, Iceland. In: Analyzed by Video Monitoring and Topographic Mapping. <https://doi.org/10.3389/feart.2018.00235>.

Wolfe, E.W., Neal, C.A., Banks, N.G., Duggan, T.J., 1988. Geologic observations and chronology of eruptive events. In: Wolfe, E.W. (Ed.), *The Pu'u O'o Eruption of Kilauea Volcano, Hawai'i: Episodes 1 through 20, January 3, 1983, through June 8, 1994*. U.S. Government Printing Office, Washington, pp. 1–97. <https://doi.org/10.3133/pp1463>.